A Global Climatology of Tropical Cyclone Eyes

KENNETH R. KNAPP

NOAA/National Centers for Environmental Information, Asheville, North Carolina

CHRISTOPHER S. VELDEN AND ANTHONY J. WIMMERS

Cooperative Institute for Meteorological Satellite Studies, University of Wisconsin–Madison, Madison, Wisconsin

(Manuscript received 13 November 2017, in final form 4 May 2018)

ABSTRACT

Intense tropical cyclones (TCs) generally produce a cloud-free center with calm winds, called the eye. The Automated Rotational Center Hurricane Eye Retrieval (ARCHER) algorithm is used to analyze Hurricane Satellite (HURSAT) B1 infrared satellite imagery data for storms occurring globally from 1982 to 2015. HURSAT B1 data provide 3-hourly observations of TCs. The result is a 34-yr climatology of eye location and size. During that time period, eyes are identified in about 13% of all infrared images and slightly more than half of all storms produced an eye. Those that produce an eye have (on average) 30 h of eye scenes. Hurricane Ioke (1992) had the most eye images (98, which is 12 complete days with an eye). The median wind speed of a system with an eye is 97 kt ($50\,\mathrm{m\,s^{-1}}$) [cf. 35 kt ($18\,\mathrm{m\,s^{-1}}$) for those without an eye]. Eyes are much more frequent in the Northern Hemisphere (particularly in the western Pacific) but eyes are larger in the Southern Hemisphere. The regions where eyes occur are expanding poleward, thus expanding the area at risk of TC-related damage. Also, eye scene occurrence can provide an objective measure of TC activity in place of those based on maximum wind speeds, which can be affected by available observations and forecast agency practices.

1. Introduction

Tropical cyclones (TCs) are some of the most destructive storms, yet at their core they are a paradox. Amidst the fury of hurricane-force winds, torrential rains, and storm surge flooding, they have a calm center with often clear skies: the eye of the storm. While much has been written about eye development and formation (e.g., Abdullah 1954; Smith 1980; Vigh et al. 2012; Willoughby et al. 1982), structure (e.g., Kossin and Schubert 2004; Schubert et al. 2007; Shapiro and Willoughby 1982), thermodynamics (Willoughby 1998), and life cycle (e.g., Malkus 1958; Sitkowski et al. 2011), there is less information available on their frequency. How often do eyes occur? Where do they occur most frequently? How does their size vary? This paper seeks to describe a climatology of the frequency, distribution, and size of TC eyes.

Vigh et al. (2012) described hurricane eyes based on 20 years (1989–2008) of aircraft reconnaissance flights in the North Atlantic. They described how often eyes occur (58% of systems had an eye identified during aircraft reconnaissance while 61% had an eye identified by infrared satellite imagery), when they first form a closed eye (about 45 h after becoming a tropical storm), and their intensity at first observed eye (mean intensity was 58 kt; $1\,\mathrm{kt} = 0.5144\,\mathrm{m\,s^{-1}}$). Because the effort used aircraft reconnaissance, they could compare when the eye was first denoted by aircraft versus infrared (IR) satellite imagery (about 15 h between the first aircraft closed eye and the first IR eye scene). Also, Cossuth (2014) developed a large set of eye fixes using the Automated Rotational Center Hurricane Eye Retrieval (ARCHER) algorithm (Wimmers and Velden 2010, 2016) and microwave imager data while studying the TC inner-core structure. However, the use of twice-daily polar orbiter microwave imagery limits the ability to diagnose certain aspects of TC eyes (e.g., frequency) in the early years of its availability (e.g., 1980s). Our work complements Vigh et al. (2012) and Cossuth (2014) by expanding the analysis in both time and space with satellite data available on a regular (3 hourly) basis.

Denotes content that is immediately available upon publication as open access.

Corresponding author: Kenneth R. Knapp, ken.knapp@noaa.gov

Herein, an automated algorithm was used to determine the center of a TC for a temporally and spatially homogeneous satellite dataset. The ARCHER algorithm estimates the TC center from the morphological features. It also provides information on the eye probability, size, completeness, and more. ARCHER was used to analyze 34 years (1982–2015) of TC imagery from the Hurricane Satellite (HURSAT) data. The global coverage and long time series provided an opportunity to investigate the climatology of tropical cyclone eyes.

2. Background and methods

a. HURSAT

The HURSAT dataset was initially developed to produce a homogeneous analysis of storm intensity through time (Knapp and Kossin 2007; Kossin et al. 2013, 2007a). It has also been used in development of TC size climatology (Knaff et al. 2014), objective intensity estimation (Fetanat et al. 2013; Jaiswal et al. 2012), evaluation of model reanalyses (Kossin 2015), and studies of cloud clusters (Lacewell and Homaifar 2015; Zawislak and Zipser 2010). HURSAT provides geostationary satellite imagery centered on TCs in the International Best Track Archive for Climate Stewardship (IBTrACS) dataset (Knapp et al. 2011).

HURSAT data provide 3-hourly observations of the infrared window channel (approximately 11 μm), providing observation of cloud tops and surface skin temperatures (depending on the presence of clouds). HURSAT imagery is provided at the same spatial scale through time; all data are subsampled to approximately 8 km. While there have been some improvements in geostationary IR spatial resolutions (e.g., 8 to 4 km) for some satellites, the resampling provides a uniform sampling of storm features.

HURSAT, version 6 (Knapp and Kossin 2017), provides data from 1979 to 2015, though this analysis begins in 1982 since that is when the global coverage of HURSAT is more complete. During this period, there were 369 330 images that were analyzed; many scenes of which were simultaneous views from separate geostationary satellites. We excluded such duplicate observations, so the climatology results from 227 760 individual images.

b. ARCHER

The ARCHER algorithm can (Wimmers and Velden 2016) estimate the center of a tropical cyclone in a satellite image using visible, infrared, or microwave data. The ARCHER algorithm was applied to all IR imagery in HURSAT B1, version 6; ARCHER parameters are

also available in HURSAT. This paper analyzes four of these parameters:

- eye radius—the radius of the eye,
- eyewall radius—the radius of the eyewall clouds,
- eye completeness—the percent of the eye that the eyewall encompasses, and
- eye probability—the probability that the scene is an eye.

Most of these parameters were developed separately from the Wimmers and Velden (2016) study but have been monitored over years of operational use in support of various real-time TC estimation schemes, such as the advanced Dvorak technique (Olander and Velden 2007). They are constructed as follows. Eye radius results from ARCHER's iterative search for the circular ring that fits the highest average gradient along the TC image's eye. Eyewall radius is the radius out from the ARCHER center fix that contains the pixel with the lowest brightness temperature, no less than the eye radius and no more than the eye radius + 0.3°. (This is very effective at the 85–92-GHz microwave frequencies and is also useful as a proxy in the infrared.) The eye completeness is the greater of two numbers: 1) the fraction that is at least 20 K cooler than the warmest pixel in the eye, or 2) the fraction of the circle associated with the eyewall radius that is cooler than 232 K. The second option ensures that an eye structure is not discounted in cases where the eye is heavily obscured.

The eye probability is a probability constructed from two years of North Atlantic data manually sorted into "eye" and "no eye" cases, and calibrated to a function of ARCHER's internal variables "confidence score" and "ring score." An eye that is partially obscured by cirrus will normally still register as having a high probability but the level of probability depends on the opacity of the cirrus. A TC with a full central dense overcast will not register a meaningful ARCHER ring score and will yield a low eye probability. Likewise, the eye probability depends on the ring score and not some minimum number of eye pixels, rather how ring-like is the cloud pattern. This approach provides less dependence on any changes in image resolution since storm features are provided at the same 8-km scale throughout the record. More details are provided by Wimmers and Velden (2010, 2016). It should also be noted that this is not the first application of ARCHER to HURSAT because Kossin et al. (2013) used the advanced Dvorak technique, which includes ARCHER analyses. This, however, is a more thorough analysis of the aspect of the TCs called "eye scenes" using ARCHER version 2.

A time series of the eye parameters is provided for Hurricane Isabel (2003) in Fig. 1. Hurricane Isabel
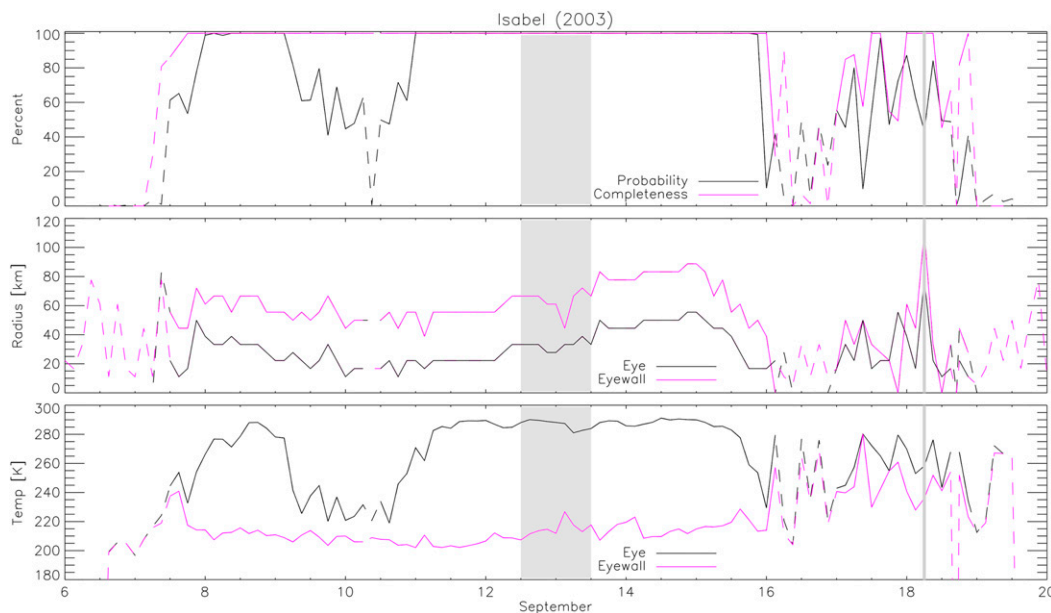
FIG. 1. Time series of ARCHER parameters for Hurricane Isabel (2003): (top) eye probability and eyewall completeness, (middle) eye and eyewall radius, and (bottom) the maximum satellite brightness temperature in the eye and eyewall. Solid lines denote when the storm likely had an eye, with dashed lines when it did not. Gray areas on 13 and 16 Sep 2003 represent eyewall replacement and landfall, respectively.

developed over the North Atlantic on 6 September 2003, made landfall on the U.S. East Coast on 18 September, and dissipated as it continued over land on 20 September. Also, it underwent an eyewall replacement cycle (ERC) from 12 to 13 September (Bell and Montgomery 2008). The system had numerous scenes that were a high probability eye scene, especially during a 5-day span from 11 to 16 September. During that span, the eye remained much warmer than the eyewall. Also, the eye and eyewall radius expanded from 20 and 50 km, respectively, to 50 and 80 km, respectively, coincident with the ERC.

Figure 2 provides some eye scenes from HURSAT as identified by ARCHER. There are scenes easily identified as characteristic eye scenes and some that are not. The Isabel image is from 11 September, prior to the ERC. Hurricane Allen (1980) has one of the smallest eyes in HURSAT; the eye and eyewall radii in this scene are only 10 and 30 km, respectively. Conversely, Hurricane Blanca (2015) had one of the largest eye radii in the record at 80 km. Typhoon Haiyan (2013) had the largest difference between the maximum eye temperature (289 K) and the eyewall temperature (192 K), which occurred when the system was near maximum intensity with a minimum central pressure of 895 hPa. These storms represent the iconic eye scenes: cold circular clouds surrounding a warm center.

Other scenes, however, represent borderline eyes or misidentified eyes, demonstrated by the images of

Hurricanes Hector and Daniel. The scene of Hurricane Hector (2006) on 18 August 2006 meets the minimum criteria for an eye (to be discussed in the next section), with a probability of 5% and an eye completeness of 100%, and is likely an eye scene. Conversely, the Hurricane Daniel (2000) image on 24 July 2000 has the same parameters (5% probability and 100% completeness) but is not likely an eye. HURSAT imagery is continuous, so inevitably it captures scenes at times of transition from noneye to eye (or vice versa). Given the variations in eye scene appearance for similar parameters, it is necessary to derive thresholds for discriminating eye scenes from non-eye scenes to understand the uncertainty of the climatology.

c. ARCHER eye detection evaluation

The ARCHER algorithm parameters were compared with results from the Cyclone Center project (www.cyclonecenter.org), which is a citizen science project where visitors to the website can provide information on the interpretation of satellite imagery of historical tropical cyclones (Hennon et al. 2015). The site uses imagery from HURSAT B1. The ability to classify TCs by scene type using Cyclone Center data and a learning algorithm was analyzed by Knapp et al. (2016), where they found that the determination of the eye scene has a Heidke skill score of 0.87. Therefore, we use the Cyclone Center data to compare its classification of scene type (eye vs no eye) with ARCHER. In addition to ARCHER eye
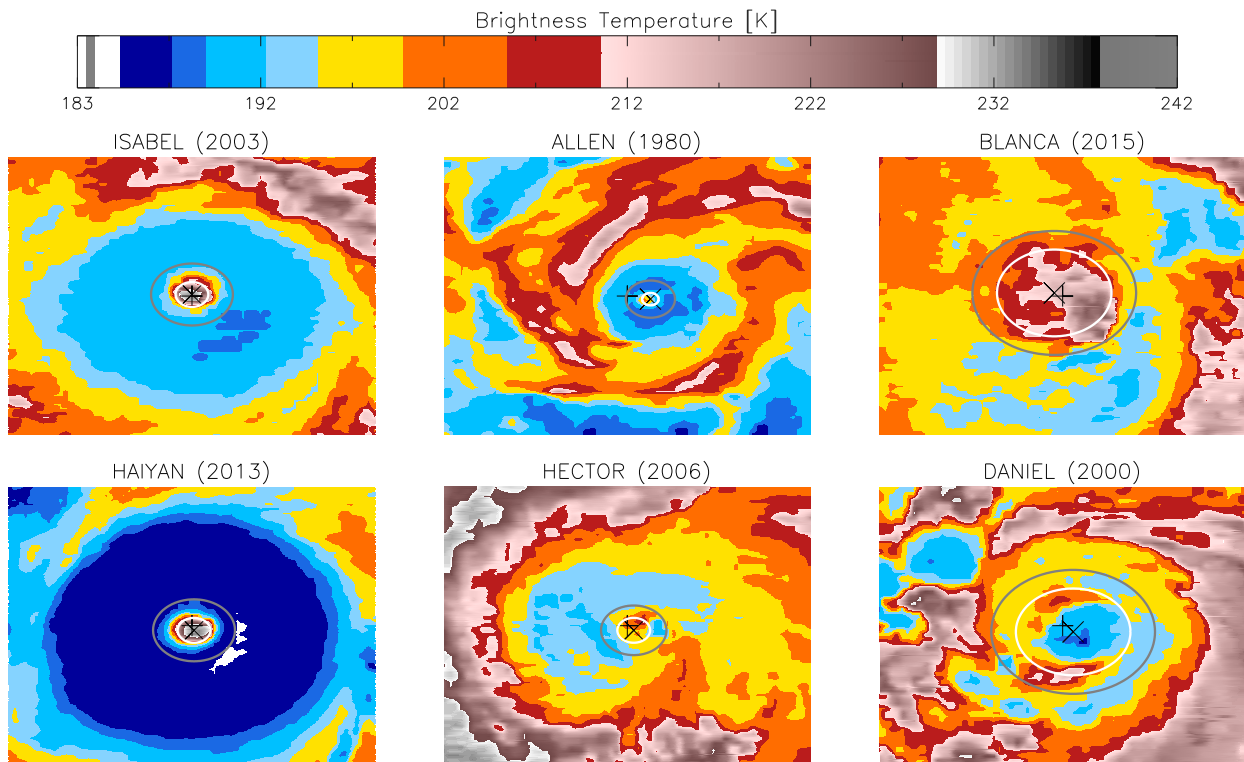
FIG. 2. Eye image samples from HURSAT as identified by ARCHER where the plus (+) sign is the image center (from interpolated best track), the crisscross (×) is the circulation center from ARCHER, the white circle is the extent of the eye, and the gray circle is the eyewall. The scale of each image is the same: 555 km (i.e., 5° latitude).

probability, the ARCHER eye completeness value was investigated to determine if it helped identify eye scenes. Thresholds for both parameters were varied such that scenes exceeding both thresholds were considered eye scenes; the resulting skill scores when compared to the Cyclone Center algorithm are shown in Fig. 3. When ARCHER eye probability is greater than 50%, the skill scores decrease as probability increases with little dependence on eye completeness. This results from the increased number of missed eyes when setting the eye probability threshold too high. At eye probabilities below 50%, there is a dependence on eye completeness, with more complete eyes aligning more closely with Cyclone Center classifications. The maximum skill score identified is 0.75, when assigning a scene as an eye when eye probability is greater than 5% and eye completeness is greater than 95%. The resulting performance of this threshold classification model is provided in Table 1 for 17 616 scenes.

The ARCHER and Cyclone Center algorithms agree on 95% of the classifications: 86% that are not eye and 9% that are eye scenes. The total eye fraction was similar for both algorithms, with ARCHER classifying 11.7% as eye scenes compared to 11.1% from the

Cyclone Center. There was disagreement on only 5% of image scenes.

d. Indian Ocean coverage gap

The source satellite data for HURSAT are ISCCP-B1 (Knapp 2008). The geostationary satellite data available
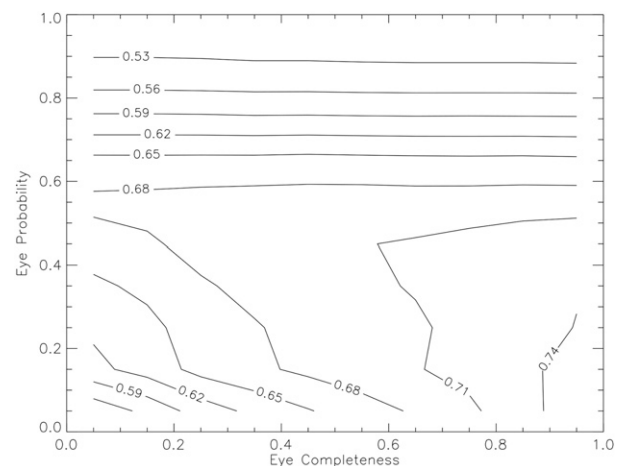

FIG. 3. Skill score as a function of eye probability and completeness thresholds for determining eye scenes.

TABLE 1. Performance of the scene classification model from ARCHER parameters compared to the scene classification from Cyclone Center (CC).

	ARCHER = eye	ARCHER = not eye
CC = eye	1564	385
CC = not eye	503	15 164

to ISCCP did not include any geostationary observations over the Indian Ocean until 1998. Prior to that, the views of that region were at-large view zenith angles (VZA), demonstrated in Fig. 4. The Gridded Satellite (GridSat; Knapp et al. 2011) image from 10 March 1994 over the south Indian Ocean shows the limits of the satellite coverage in this area. The gap (white region) at 70°E is a region not visible from the geostationary satellites at 0° and 140°E. Intense Tropical Cyclone Litanne (1994) can be seen near the image seam at 70°E. The close-up image of Litanne shows that in spite of a 74° VZA, an eye is still apparent. This is not the case for all cyclones in this region, particularly for smaller eyes.

We can investigate the impact of these higher view zenith angles because the European *Meteorological Satellite-5* (*Meteosat-5*) was moved to the Indian Ocean data coverage (IODC) position at 63°E in 1998. We provide statistics of the numbers of eye scenes in the south Indian and north Indian basins with and without the IODC in Table 2, where an eye storm is defined as a TC with at least one eye scene. Both the mean number of eye scenes in an eye storm and the maximum number of eye scenes in a storm decrease without IODC in both basins. Thus, when there is no satellite in IODC, fewer eye scenes were identified. However, the fraction of eye storms (the fraction of storms with at least one eye

scene) does not likewise decrease but increases in the northern Indian basin and decreases in the southern Indian basin. Thus, the known impact of adding IODC in 1998 on a global eye climatology is a small increase in eye scenes, while the impact on the number of observed eye storms is unclear because of different responses (positive and negative) in the two basins.

e. Caveats

It should be noted that there are some limitations with this climatology that should be considered when interpreting the results. The ARCHER algorithm has historically been applied to 4-km IR data but is used with 8-km data here. Therefore, there will be some missed eye scenes in this climatology for storms with very small eyes. Also, the climatology is limited to the HURSAT period of record, which spans 1982–2015 for this study.

The eye scenes are flagged objectively with a skill score of 0.75. Thus while good, it is not perfect and there will be times when an eye is missed or a scene is mislabeled as an eye. Furthermore, while many scenes are eye or not eye scenes, there are some scenes where it just is not apparent (cf. Fig. 2). Based on Table 1, there is agreement on about 95% of all scenes.

This climatology uses IR imagery only. A significant advantage of the B1 data is their consistent 3-hourly observations for nearly all TCs. However, microwave imagery can identify eye scenes earlier in a storm's lifetime or when an eye is obscured by cirrus (Cossuth 2014; Velden et al. 2006; Vigh et al. 2012). Microwave observations come at the sacrifice of temporal coverage (starts in 1989) and resolution (only twice daily in the early years). Thus, it should be understood that some of the statistics discussed below (e.g., time of formation of
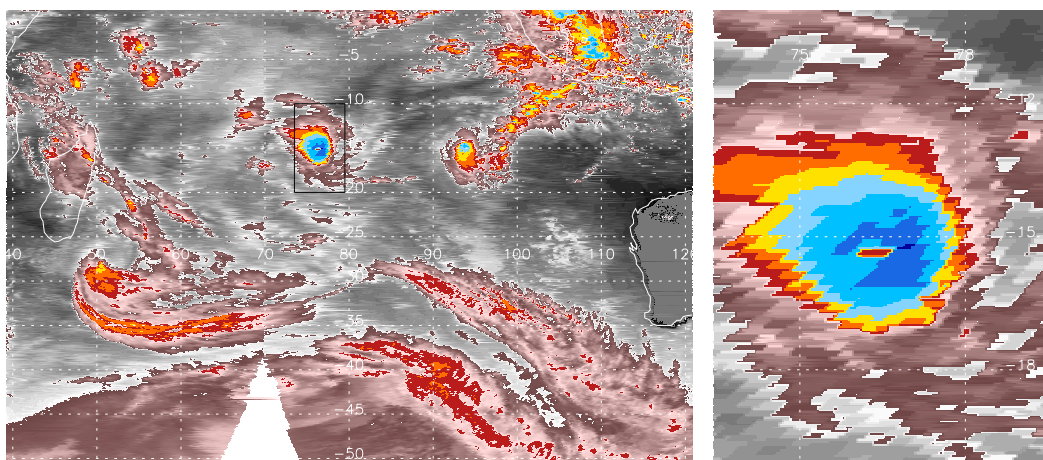

FIG. 4. (left) GridSat image of the southern Indian Ocean from 10 Mar 1994 and (right) close up of Tropical Cyclone Litanne (1994) (box in plot on left), using the same color scale as Fig. 2.

TABLE 2. Eye scene statistics with and without Indian Ocean data coverage (IODC) for 1999–2015.

	North Indian Ocean		South Indian Ocean	
	IODC	Without IODC	IODC	Without IODC
Eye scene fraction	2.4%	1.8%	3.0%	1.9%
Eye storm fraction	19.3%	21.2%	22.2%	18.6%
Mean No. of eye scenes	4.6	3.1	7.3	6.7
Max No. of eye scenes	30	19	49	31

first eye scene) would be different were microwave analysis combined with this IR dataset.

Last, there is limited coverage of the Indian Ocean during the early portion of the record (1982–97). From the analysis above, the impact is more noticeable on the number of eye scenes in a storm with less impact on determining the presence of an eye for a given storm.

3. Eye climatology

Figure 5 shows the distribution of TC maximum wind speeds for all TC scenes separated by eye versus non-eye scenes (using 1-min maximum sustained winds from IBTrACS). The median wind speed for eye and non-eye scenes is 97 and 35 kt, respectively. Based on Dvorak (1984), TCs with eyes generally have winds at 65 kt or higher. This can be seen in the figure, where the eye frequency increases sharply at the 50–70-kt range. At 100 kt, the eye scenes become more frequent than non-eyes. Thus, a storm with winds greater than 100 kt are the most likely to have an eye scene and the fraction reaches 100% at 160 kt though the number of storms at this intensity are few (the large decrease at 170 kt is caused by the few storms sampled, there are only 3 storms at this intensity).

The following sections analyze the frequency and spatial distribution of TC eyes. Also, given the average intensity of eye storms, it is important to understand any possible temporal changes in the eye scene frequency or spatial distribution that may be detectable with this data, since any such changes would have significant impact on local populations.

a. Eye scene frequency

The images labeled as eye scenes compose 12.6% of all HURSAT imagery. On a per storm basis, 51% of all storms had at least one eye scene, hereafter called eye storms. There seem to be some marginal eye storms since those with exactly one eye scene account for 13% of all storms, meaning 38% of cyclones have two or more eye scenes.

The average eye storm has 10 eye scenes over its life cycle, which is just over a day (given 3-hourly data). The distribution has a large tail; the 75th and 95th percentiles for number of eye scenes is 16 and 36, respectively, and storms exist that go far beyond the 95th percentile.

Table 3 lists the 10 storms with the most eye scenes. We have also included the Southern Hemisphere storm with the most eye scenes for perspective. Hurricane Ioke (2006) stands out from the rest with 98 eye scenes—a cumulative 12 days as an eye storm. The difference in number of eye scenes from Ioke to Isabel (i.e., first to second) is as large as the span from second to 30th. These top 10 storms occur in the North Atlantic and North Pacific (both eastern and western).

The time series of eye scene and eye storm fraction are provided in Fig. 6. Neither series has a statistically
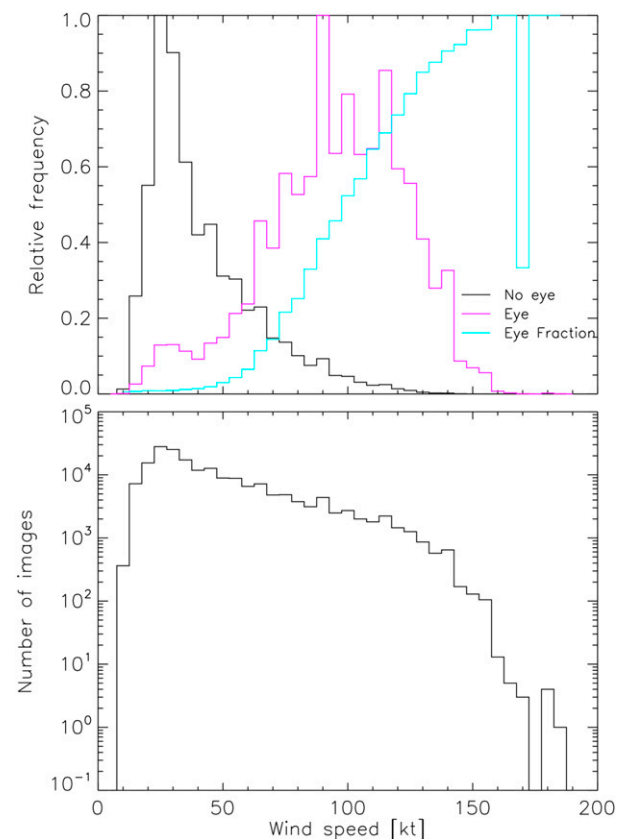

FIG. 5. (top) Histogram of 1-min maximum sustained wind speeds for scenes without an eye (black) and with an eye (magenta) along with the fraction of storms with detectable eyes at each wind speed (cyan). (bottom) Distribution of TC wind speeds for analyzed HURSAT images.

TABLE 3. The 10 storms with the most eye scenes from 1982 to 2015 along with the top storm from the Southern Hemisphere.

Rank	No.	Name	Year	Basin(s)
1	98	Ioke	2006	EP, WP
2	73	Isabel	2003	NA
2	73	Luis	1995	NA
4	72	John	1994	EP, WP
5	70	Ivan	2004	NA
6	69	Trudy	1990	EP
7	67	Seth	1991	WP
8	63	Fengshen	2002	WP
9	62	Gert	1999	NA
9	62	Kevin	1991	EP
31	49	Kalunde	2003	SI

significant trend from 1982 to 2015, so it appears that the frequency of eye scenes or storms is not changing. Also, the two time series are not well correlated ($R^2 = 0.21$). The year with the most eye scenes (2015 with 18.5%) does not correspond to the year with the most eye storms (1992 when 62% of storms had eyes).

The frequency of eye scenes during a storm's lifetime is plotted in Fig. 7. Eye scenes are most numerous just after the fifth day of a storm's existence. While the number of eyes approach zero after day 15, the decrease in the fraction of storms is abated because there are few storms with long lifetimes. So after a storm's 10th day, there is roughly a 1 in 10 chance that the current scene has an eye. The tail disappears when normalizing time to the life of the system. In Fig. 8, the eyes are numbered relative to their position between the first and last observation point of a storm. In this case, 50% of the eye scenes occur between 0.38 and 0.64. In fact, 80% of all eyes scenes occur during the middle half (from 0.25 to 0.75) of a storm's lifetime.

For eye storms, the eye first appears within the first 6.6 days of tracking the system (regardless of initial intensity) for 90% of the systems. The time from when the storm first reaches 34 kt to the first eye is less than 4.25 days for 90% of the storms and 50% of systems have their first IR eye within 2 days of being named. Thus, the value of roughly 45 h (or 2 days) from naming a North Atlantic system to the first eye observed with aircraft by Vigh et al. (2012) is consistent with the global value found here with satellites.

b. Eye scene spatial distribution

Figure 9 shows the spatial distribution of tropical cyclones in this study and the fraction of which have eye scenes (data are binned in 5° boxes and eye storm fraction is only shown when there are more than 100 scenes per box). Eye scenes are most frequent in the western Pacific (WP), specifically in a large region between Japan and the Philippine Islands, where 37% of the
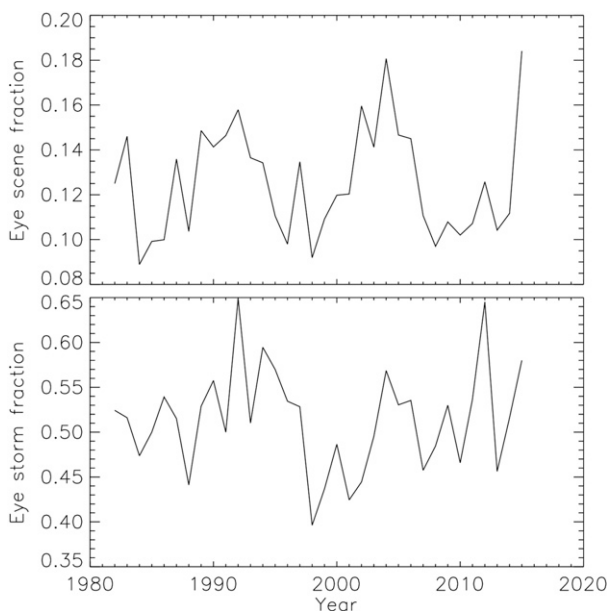

FIG. 6. Annual time series of fraction of HURSAT images identified as (top) eye scenes and (bottom) eye storms.

scenes are eye storms. While the highest density of storms is in the eastern Pacific (EP), the percentage of eye systems is not as profound, with values near 18%. Over the North Atlantic (NA), eye scenes are most frequent in the open North Atlantic (with a maximum near 28%), values are lower closer to the United States and the maximum in the Gulf of Mexico only reaches 17%. Eyes are much less frequent in the Southern Hemisphere, which is consistent with Table 3. The maximum in the south Indian basin (SI) occurs between La Reunion Island and Madagascar (16%) and the maximum southeast of Samoa in the South Pacific (SP) is only 15%.

The summary of eye frequency for each basin is provided in Table 4. In terms of the fraction of all scenes, there are three basins above average (western Pacific, eastern Pacific, and North Atlantic). Conversely, the north Indian (NI) and the Southern Hemisphere basins were below the global average of 12.6% of scenes. For the eye storm fraction, while the western and eastern Pacific are still above average, the North Atlantic is near the minimum (41%). Thus, with a large fraction of eye scenes spread across proportionately fewer storms, the mean number of eye scenes in an eye storm is near the maximum in the North Atlantic (12.6 per storm). Only by a small margin does the prolific western Pacific have more eye scenes per storm (12.8) than the North Atlantic. The rest of the basins are below average in terms of mean number of eye scenes. The most eye scenes in a storm for a given basin vary from 30 in the north Indian to 98 for Hurricane Ioke. It should be noted
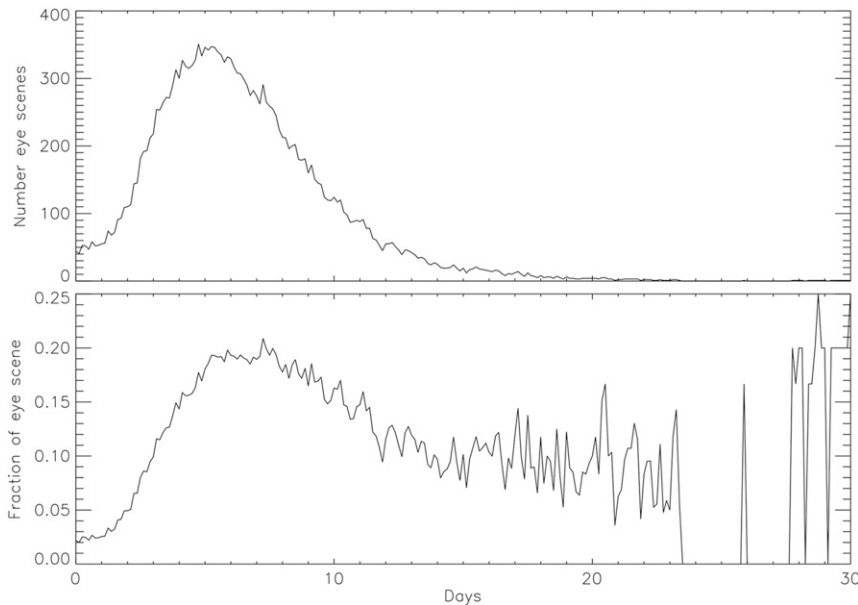
FIG. 7. (top) Number of eye scenes and (bottom) fraction of storms that have eyes as a function of storm lifetime (in days since first best track position).

that the 98 eye scenes were split between the eastern and western Pacific (with 36 and 62 eye scenes, respectively).

In addition to the general distribution of eye scenes, the 34 years of data provide the ability to look at potential changes in the location of the eye scenes. Figure 10 provides the quantile regression of the location of eye scenes. The location of the first occurrence of an eye remains relatively unchanged through time. However, the location of all eyes is shifting poleward. The overall rate is approximately $0.045°$ latitude yr^{-1}. Separating the analysis by hemisphere (not shown) produces expansion rates of $0.05°$ and $0.025°$ latitude yr^{-1} in the Northern and Southern Hemisphere, respectively. So it appears the combined expansion away from the pole is roughly $80 \, km \, decade^{-1}$. The rate appears to be higher for eyes occurring near the edge of the tropics (around $23°$). The location of the last eye scene of a system is also moving poleward. The overall linear regression is significant at $p = 0.05$ with the largest contribution coming from eyes just outside the tropics (between $22°$ and $28°$). This is consistent with Kossin et al. (2014), who find that the location of a TC's lifetime maximum intensity (LMI) is expanding poleward at a slightly larger rate ($\sim 118 \, km \, decade^{-1}$). However, the trend of poleward expansion in Fig. 10 derives from objectively identified eye scenes rather than position of maximum storm intensity. In summary, there appears to be an expansion of the region of the tropics that are prone to eye storms, which is consistent with a previous study, with the equatorward boundary remaining somewhat stationary and the poleward boundary moving poleward.

c. Eye size

Kossin et al. (2007b) find a correlation between eye radius and radius of maximum winds. Thus, the eye size data in HURSAT can help estimate hurricane wind structure where few measurements exist globally. The
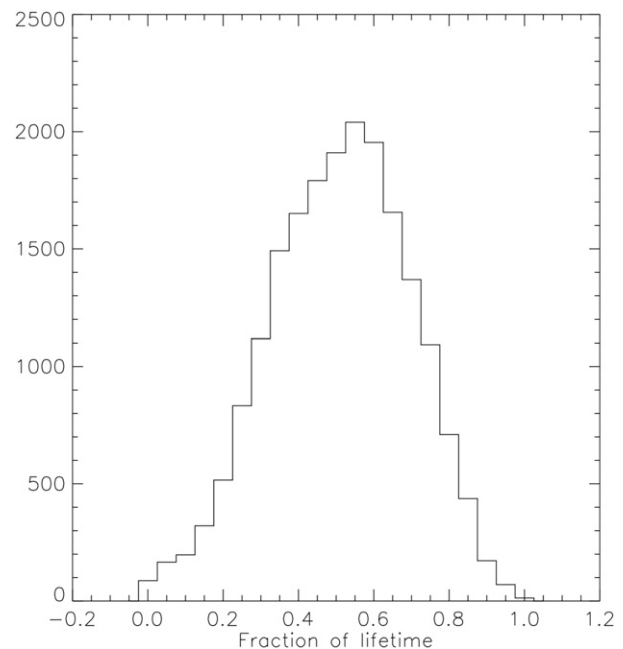

FIG. 8. Number of eye scenes as a function of storm lifetime [normalized from first reported position ($T = 0$) to last reported position ($T = 1$)].
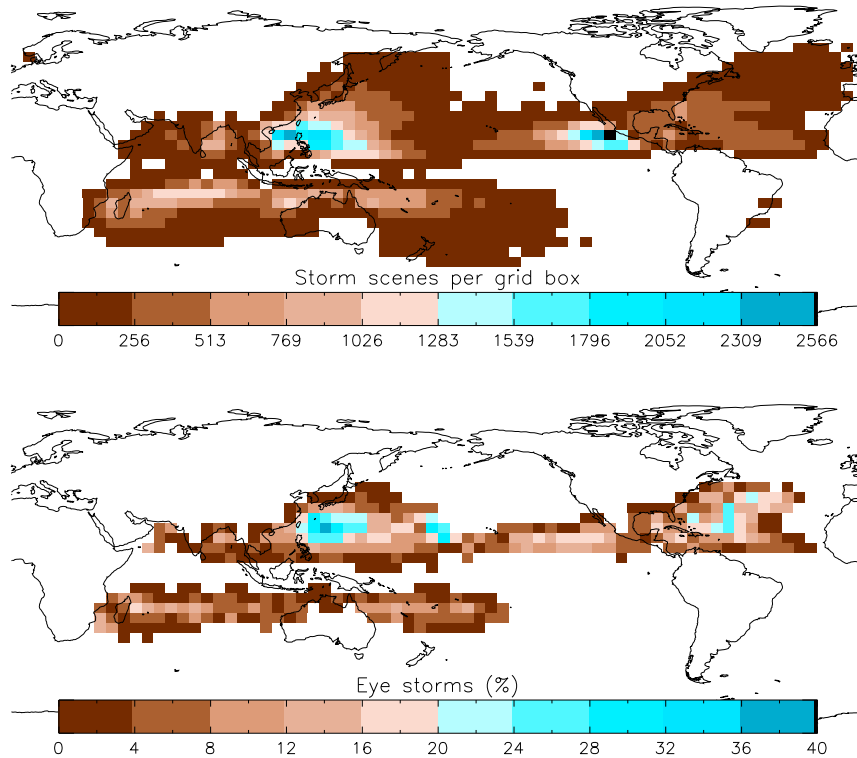
FIG. 9. (top) Number of storm scenes in each 5° box. (bottom) Percent of scenes that are eyes (only showing percentages when number of scenes per box exceeds 100).

histograms of eye and eyewall size are shown in Fig. 11. The mean eye radius is 26 km, with a 75th and 90th percentiles at 28 and 50 km, respectively. The detection limit of the ARCHER algorithm using HURSAT data appears to be about 10 km. This is consistent with the HURSAT pixel size of about 8 km.

Eye size does vary spatially (as shown in Table 5). The Southern Hemisphere, while having far fewer eye scenes, has larger eyes. The mean eye radii for the south Indian and South Pacific are 34 and 37 km, respectively, both of which are larger than the global average. The eastern Pacific is the basin with the smallest average eye size (22 km). In the Northern Hemisphere, the western Pacific has the largest mean eye size (though only marginally larger than the north Indian). The distribution of eyewall radius is also provided in Fig. 11. The mean eyewall size is 54 km. The eyewall sizes appear to be

proportional to the eye size (not shown), with the same rank ordering of basin sizes.

4. Eye scenes and annual TC activity

The global annual TC activity is measured in various ways: numbers of storms, accumulated cyclone energy (ACE), potential destruction index (PDI), and more. Many of these measures are dependent on various practices (e.g., timing of the naming of a storm) and conventions (e.g., wind speed averaging periods), both of which can affect annual statistics and trends. A measure of TC activity is needed that does not depend so much on human estimates of intensity or strength, which have changed over time (Knapp and Kruk 2010) and can produce conflicting results (Emanuel 2005; Wu et al. 2006). The following investigates the relationship

TABLE 4. Statistics of eye scenes globally and by basin.

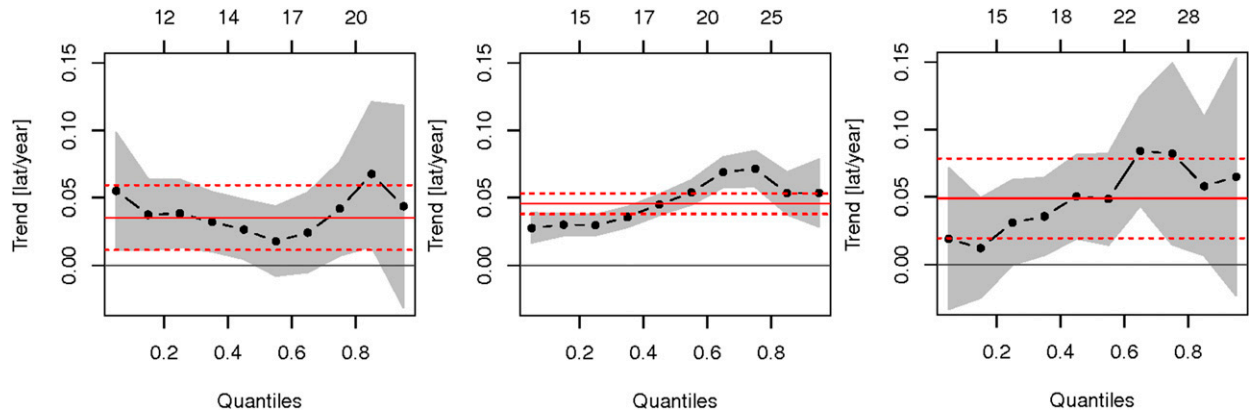|	Global	NI	WP	EP	NA	SI	SP
Eye scenes (%)	12.6	10.1	20.4	16.4	16.0	6.5	6.8
Eye storms (%)	51	46	66	52	41	43	40
Eye scene counts—mean	10.6	3.8	12.8	9.4	12.6	8.0	7.7
Eye scene counts—max	98	30	67	69	73	49	40

FIG. 10. Quantile regression of latitude of the first occurrence of (left) an eye, (middle) all eye scenes, and (right) last eye scene for each storm. The numbers on the top of the plots show the percentile values (in ° latitude), red line is the linear regression trend along with the $p = 0.05$ uncertainty (dashed red), and the shaded region denotes the $p = 0.05$ uncertainty for the quantile regression.

between occurrence of HURSAT eye scenes and two measures of activity: number of hurricane-strength TCs and number of hurricane-strength TC days. While the term hurricane is often related to TCs occurring in the Western Hemisphere, here the term is used to describe the strength of wind (e.g., hurricane-force winds).

a. A proxy for number of hurricane-strength TCs

One temporal measure of storm activity is the number of TCs that reach a given intensity. For example, the number of named storms can be counted as the number of TCs with 1-min maximum sustained wind speeds, W, greater than 34 kt. Likewise, the number of hurricanes ($W > 64$ kt) and major hurricanes ($W > 95$ kt) are used by Diamond and Schreck (2017). Similarly, a minimum threshold on the number of eye scenes for a TC can be used to count TC activity. By varying the intensity threshold and eye scene limit, one can determine an optimal set that maximizes the correlation between number of TCs based on intensity and number based on eye scenes. The optimal thresholds showed high correlation ($R = 0.81$) between storms with lifetime maximum intensity greater than 70 kt and having at least two eye scenes. Thus, it is possible to construct annual counts of "proxy hurricane-strength TCs" that are consistent between basins and through time.

b. A proxy for hurricane-strength TC days

The metric "hurricane days" is the sum of all occurrences of storms with an intensity of hurricane strength or greater (using 1-min winds) for global storm activity. It represents a measure of the activity by integrating the occurrences of strong TCs (Klotzbach 2011). This concept can be adapted globally as hurricane-strength TC (HSTC) days. The relationship between HSTC days and number of annual eyes is provided in Fig. 12, where the

correlation coefficient is 0.84. It appears that the annual number of eyes can be a proxy for HSTC days.

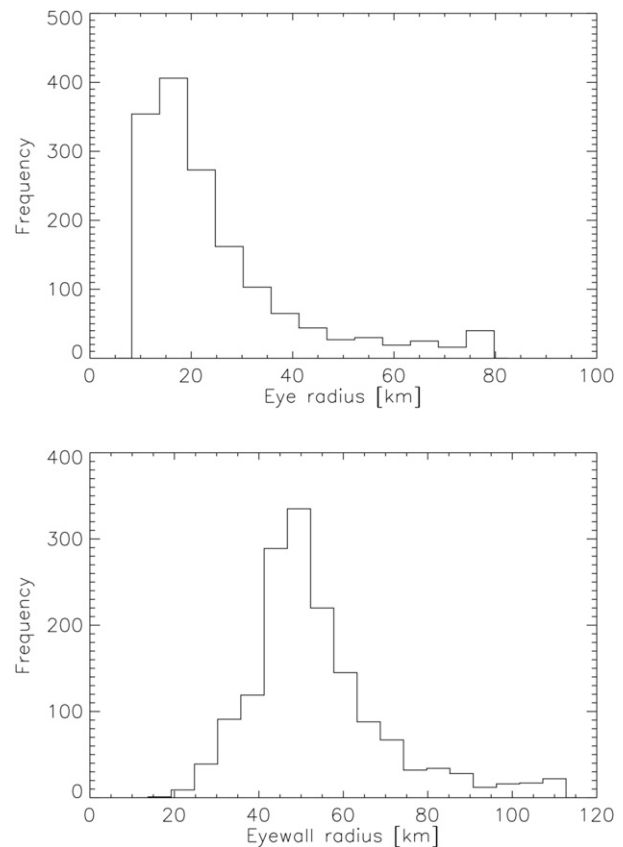The time series of the error of the proxy hurricane days (Fig. 12) shows two regimes of error: large errors

FIG. 11. Histograms of (top) eye radius and (bottom) eyewall radius.

TABLE 5. Statistics of eye and eyewall radii (km) globally and by basin.

	Global	NI	WP	EP	NA	SI	SP
Eye size—mean	26.3	25.2	25.4	22.5	23.3	34.5	37.3
Eye size—standard deviation	16.7	16.5	15.3	13.8	13.3	21.1	23.0
Percent of eyes larger than 35 km	20	19	18	12	13	37	43
Eyewall size—mean	54.1	53.1	54.7	49.9	51.1	62.2	64.1
Eyewall size—standard deviation	17.6	16.7	16.9	15.7	15.3	19.8	21.8

before 1998 and smaller errors after. The analysis was repeated using only the uniform views (i.e., ignoring satellites in the IODC) and the result is the same: a larger variation in proxy error before 1998. The errors do not seem to derive from a new satellite position over the Indian Ocean. It is not clear if the change in error characteristics results from differences in the eye scene or if there are biases in the global best track data record. HSTC days may be more temporally consistent from eye data than when derived from the best track record.

5. Summary

An established algorithm for identifying centers of tropical cyclones—and in particular, the characteristics related to eyes—is applied to a long-term, homogenous satellite dataset of infrared imagery. One result of this application is a more complete climatology of TCs that form an eye. While previous work focused on aircraft and satellite observations in the North Atlantic and microwave imagery, this approach is global and more routinely observes the system (satellite imagery were available at 3-h intervals).

The primary results include the following:

- 12.6% of all infrared TC image scenes are identified as eye scenes.
- 51% of all TCs from 1982 to 2015 had at least one eye scene.
- The median wind speed for TCs with an eye scene was 97 kt versus 35 kt for noneye scenes.
- The average eye storm spent 30 h (10 scenes) as an eye but many storms have more eyes, with Hurricane Ioke having by far the most eye scenes: 98 (more than 12 days with an eye).
- Eye scenes are most numerous just after the fifth day of a storm's existence.
- The time from when the storm first reaches 34 kt to the first eye is less than 4.25 days for 90% of the storms and 50% of systems have their first IR eye within 2 days of being named, which is consistent with regional studies using aircraft data.
- Eye scenes are much more numerous in the Northern Hemisphere, with a region in the western Pacific being

the most prolific (where 37% of the scenes are eye scenes).
- The zonal region that is prone to experiencing eye storms is expanding poleward.
- The mean eye radius is 26 km and, on average, eye sizes in the Southern Hemisphere are larger than the Northern Hemisphere.
- Annual numbers of eye storms and eye scenes can be used as proxies for number of hurricane-strength TCs and hurricane-strength TC days, respectively.
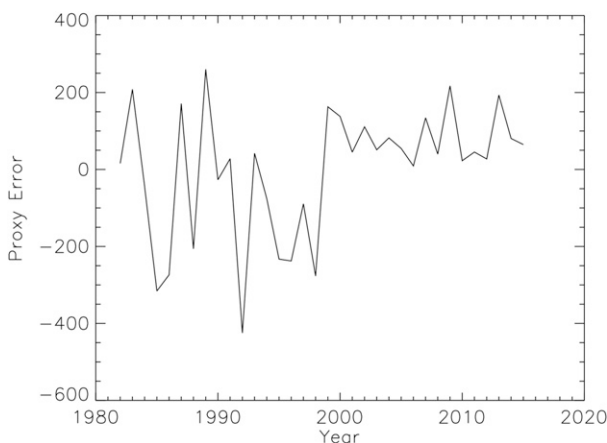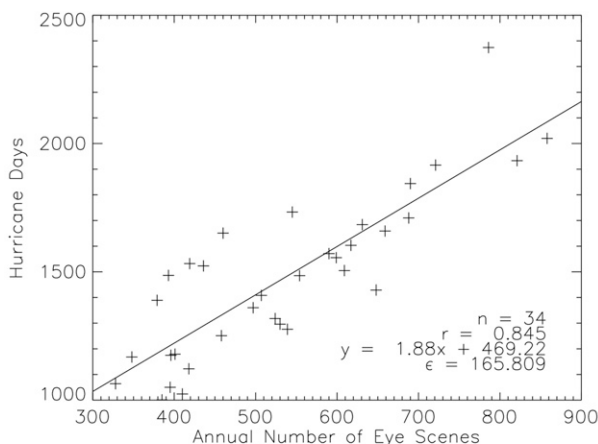

FIG. 12. (top) Global hurricane days vs annual number of eye scenes, linear regression information is provided in the legend. (bottom) Linear regression error vs time.

- The number of hurricane-strength TC days shows large variation in early years (1982–97) suggesting some temporal inhomogeneities, at least in relationship to the number of eye scenes.

While this effort has some limitations, it represents a thorough analysis of 34 years of tropical cyclones. Further improvements could be made by incorporating microwave (MW) data and AVHRR data, and producing a consensus eye product that incorporates all satellite data. Also, much more can be done with the ARCHER and HURSAT data stored together to better understand relationships between storm morphology, structure, and intensity.

REFERENCES

Abdullah, A. J., 1954: A proposed mechanism for the development of the eye of a hurricane. *J. Meteor.*, **11**, 189–195, https://doi.org/10.1175/1520-0469(1954)011<0189:APMFTD>2.0.CO;2.

Bell, M. M., and M. T. Montgomery, 2008: Observed structure, evolution, and potential intensity of category 5 Hurricane Isabel (2003) from 12 to 14 September. *Mon. Wea. Rev.*, **136**, 2023–2046, https://doi.org/10.1175/2007MWR1858.1.

Cossuth, J. H., 2014: Exploring a comparative climatology of tropical cyclone core structures. Ph.D. dissertation, Department of Earth Ocean and Atmospheric Science, Florida State University, 185 pp., http://purl.flvc.org/fsu/fd/FSU_migr_etd-8965.

Diamond, H. J., and C. J. Schreck III, 2017: The tropics [in "State of the Climate in 2016"]. *Bull. Amer. Meteor. Soc.*, **98**, S93–S128.

Dvorak, V. F., 1984: Tropical cyclone intensity analysis using satellite data. National Oceanic and Atmospheric Administration/National Environmental Satellite, Data, and Information Service, 47 pp.

Emanuel, K., 2005: Increasing destructiveness of tropical cyclones over the past 30 years. *Nature*, **436**, 686–688, https://doi.org/10.1038/nature03906.

Fetanat, G., A. Homaifar, and K. R. Knapp, 2013: Objective tropical cyclone intensity estimation using analogs of spatial features in satellite data. *Wea. Forecasting*, **28**, 1446–1459, https://doi.org/10.1175/WAF-D-13-00006.1.

Hennon, C. C., and Coauthors, 2015: Cyclone Center: Can citizen scientists improve tropical cyclone intensity records? *Bull. Amer. Meteor. Soc.*, **96**, 591–607, https://doi.org/10.1175/BAMS-D-13-00152.1.

Jaiswal, N., C. M. Kishtawal, and P. K. Pal, 2012: Cyclone intensity estimation using similarity of satellite IR images based on histogram matching approach. *Atmos. Res.*, **118**, 215–221, https://doi.org/10.1016/j.atmosres.2012.07.006.

Klotzbach, P. J., 2011: Forecasting October–November Caribbean hurricane days. *J. Geophys. Res.*, **116**, D18117, https://doi.org/10.1029/2011JD016146.

Knaff, J. A., S. P. Longmore, and D. A. Molenar, 2014: An objective satellite-based tropical cyclone size

climatology. *J. Climate*, **27**, 455–476, https://doi.org/10.1175/JCLI-D-13-00096.1.

Knapp, K. R., 2008: Scientific data stewardship of International Satellite Cloud Climatology Project B1 global geostationary observations. *J. Appl. Remote Sens.*, **2**, 023548, https://doi.org/10.1117/1.3043461.

——, and J. P. Kossin, 2007: New global tropical cyclone data from ISCCP B1 geostationary satellite observations. *J. Appl. Remote Sens.*, **1**, 013505, https://doi.org/10.1117/1.2712816.

——, and ——, 2017: Hurricane Satellite (HURSAT) from International Satellite Cloud Climatology Project (ISCCP) B1, version 6. NOAA/National Centers for Environmental Information, accessed 7 October 2017, doi.org/10.7289/V55X274D.

——, and M. C. Kruk, 2010: Quantifying interagency differences in tropical cyclone best track wind speed estimates. *Mon. Wea. Rev.*, **138**, 1459–1473, https://doi.org/10.1175/2009MWR3123.1.

——, and Coauthors, 2011: Globally gridded satellite observations for climate studies. *Bull. Amer. Meteor. Soc.*, **92**, 893–907, https://doi.org/10.1175/2011BAMS3039.1.

——, J. L. Matthews, J. P. Kossin, and C. C. Hennon, 2016: Identification of tropical cyclone storm types using crowdsourcing. *Mon. Wea. Rev.*, **144**, 3783–3798, https://doi.org/10.1175/MWR-D-16-0022.1.

Kossin, J. P., 2015: Validating atmospheric reanalysis data using tropical cyclones as thermometers. *Bull. Amer. Meteor. Soc.*, **96**, 1089–1096, https://doi.org/10.1175/BAMS-D-14-00180.1.

——, and W. H. Schubert, 2004: Mesovortices in Hurricane Isabel. *Bull. Amer. Meteor. Soc.*, **85**, 151–153, https://doi.org/10.1175/BAMS-85-2-151.

——, K. R. Knapp, D. J. Vimont, R. J. Murnane, and B. A. Harper, 2007a: A globally consistent reanalysis of hurricane variability and trends. *Geophys. Res. Lett.*, **34**, L04815, https://doi.org/10.1029/2006GL028836.

——, J. A. Knaff, H. I. Berger, D. C. Herndon, T. A. Cram, C. S. Velden, R. J. Murnane, and J. D. Hawkins, 2007b: Estimating hurricane wind structure in the absence of aircraft reconnaissance. *Wea. Forecasting*, **22**, 89–101, https://doi.org/10.1175/WAF985.1.

——, T. L. Olander, and K. R. Knapp, 2013: Trend analysis with a new global record of tropical cyclone intensity. *J. Climate*, **26**, 9960–9976, https://doi.org/10.1175/JCLI-D-13-00262.1.

——, K. A. Emanuel, and G. A. Vecchi, 2014: The poleward migration of the location of tropical cyclone maximum intensity. *Nature*, **509**, 349–352, https://doi.org/10.1038/nature13278.

Lacewell, C. W., and A. Homaifar, 2015: Identifying developing cloud clusters using predictive features. *Machine Learning and Data Mining Approaches to Climate Science: Proceedings of the 4th International Workshop on Climate Informatics*, V. Lakshmanan et al., Eds., Springer International Publishing, 217–225.

Malkus, J. S., 1958: On the structure and maintenance of the mature hurricane eye. *J. Meteor.*, **15**, 337–349, https://doi.org/10.1175/1520-0469(1958)015<0337:OTSAMO>2.0.CO;2.

Olander, T. L., and C. S. Velden, 2007: The advanced Dvorak technique: Continued development of an objective scheme to estimate tropical cyclone intensity using geostationary infrared satellite imagery. *Wea. Forecasting*, **22**, 287–298, https://doi.org/10.1175/WAF975.1.

Schubert, W. H., C. M. Rozoff, J. L. Vigh, B. D. McNoldy, and J. P. Kossin, 2007: On the distribution of subsidence in the hurricane eye. *Quart. J. Roy. Meteor. Soc.*, **133**, 595–605, https://doi.org/10.1002/qj.49.

Shapiro, L. J., and H. E. Willoughby, 1982: The response of balanced hurricanes to local sources of heat and momentum. *J. Atmos. Sci.*,

39, 378–394, https://doi.org/10.1175/1520-0469(1982)039<0378: TROBHT>2.0.CO;2.

Sitkowski, M., J. P. Kossin, and C. M. Rozoff, 2011: Intensity and structure changes during hurricane eyewall replacement cycles. *Mon. Wea. Rev.*, **139**, 3829–3847, https://doi.org/10.1175/MWR-D-11-00034.1.

Smith, R. K., 1980: Tropical cyclone eye dynamics. *J. Atmos. Sci.*, **37**, 1227–1232, https://doi.org/10.1175/1520-0469(1980)037<1227: TCED>2.0.CO;2.

Velden, C., and Coauthors, 2006: The Dvorak tropical cyclone intensity estimation technique: A satellite-based method that has endured for over 30 years. *Bull. Amer. Meteor. Soc.*, **87**, 1195–1210, https://doi.org/10.1175/BAMS-87-9-1195.

Vigh, J. L., J. A. Knaff, and W. H. Schubert, 2012: A climatology of hurricane eye formation. *Mon. Wea. Rev.*, **140**, 1405–1426, https://doi.org/10.1175/MWR-D-11-00108.1.

Willoughby, H. E., 1998: Tropical cyclone eye thermodynamics. *Mon. Wea. Rev.*, **126**, 3053–3067, https://doi.org/10.1175/1520-0493(1998)126<3053:TCET>2.0.CO;2.

——, J. A. Clos, and M. G. Shoreibah, 1982: Concentric eye walls, secondary wind maxima, and the evolution of the hurricane vortex. *J. Atmos. Sci.*, **39**, 395–411, https://doi.org/10.1175/1520-0469(1982)039<0395:CEWSWM>2.0.CO;2.

Wimmers, A. J., and C. S. Velden, 2010: Objectively determining the rotational center of tropical cyclones in passive microwave satellite imagery. *J. Appl. Meteor. Climatol.*, **49**, 2013–2034, https://doi.org/10.1175/2010JAMC2490.1.

——, and ——, 2016: Advancements in objective multisatellite tropical cyclone center fixing. *J. Appl. Meteor. Climatol.*, **55**, 197–212, https://doi.org/10.1175/JAMC-D-15-0098.1.

Wu, M. C., K. H. Yeung, and W. L. Chang, 2006: Trends in western North Pacific tropical cyclone intensity. *Eos, Trans. Amer. Geophys. Union*, **87**, 537–539, https://doi.org/10.1029/2006EO480001.

Zawislak, J., and E. J. Zipser, 2010: Observations of seven African easterly waves in the east Atlantic during 2006. *J. Atmos. Sci.*, **67**, 26–43, https://doi.org/10.1175/2009JAS3118.1.